JOURNAL OF GENERAL VIROLOGY

RESEARCH ARTICLE

Sykora *et al.*, *Journal of General Virology* 2025;106:002168
DOI 10.1099/jgv.0.002168

MICROBIOLOGY SOCIETY

OPEN ACCESS

The architecture of membrane structures involved in hepatitis C virus genome replication revealed under close-to-native conditions by cryo-electron tomography

Upasana M. Sykora[1,2], Thomas J. O' Sullivan[1,2], Yehuda Halfon[1,2], Juan Fontana[1,2,3,*] and Mark Harris[1,2,*]

Abstract

Hepatitis C virus (HCV) infection induces extensive rearrangements of host cytoplasmic membranes, leading to the formation of multiple membranous structures that facilitate RNA replication. Current knowledge of these membranous structures has largely relied on correlative light and electron microscopy techniques using chemical fixation and resin embedding. To overcome these limitations, cryo-preserved cells were prepared using cryo-focused ion beam (cryo-FIB) milling and cryo-ultramicrotomy. For the first time, the contents within the membranous structures have been observed *in situ* using cryo-electron tomography (cryo-ET) performed on lamellae (prepared via cryo-FIB) and on ultrathin sections (prepared via cryo-ultramicrotomy) from HCV subgenomic replicon-harbouring cells. Observations from 112 cryo-electron tomograms of cryo-FIB-derived samples revealed the presence of densities within the inner vesicles of a subset of single- and double-membrane vesicles, as well as within multi-vesicular bodies, which are consistent with the presence of the viral genome replication machinery. Notably, this study also presents the first direct visualization of densities within a multi-membrane vesicle observed by cryo-electron microscopy of vitreous sections. The cryo-ET methodologies established here lay the groundwork for future investigations into the architecture of the HCV replication complex, leveraging advanced computational tools for deeper structural and functional analyses.

DATA SUMMARY

The datasets generated during and/or analysed during the current study are available from the corresponding authors upon reasonable request. Figshare supplementary material link: https://doi.org/10.6084/m9.figshare.30306745.v1 [1].

INTRODUCTION

Hepatitis C virus (HCV) is a positive-sense RNA virus that primarily infects hepatocytes in the liver, leading to both acute and chronic hepatitis. The latter results in progressive liver damage, including cirrhosis, liver failure and hepatocellular carcinoma [2]. In common with other positive-sense RNA viruses, HCV induces cytoplasmic membrane rearrangements in the host cell to form specialized structures that support genome replication [3]. Current ultrastructural insights into host membrane rearrangements during HCV infection have primarily come from fluorescence microscopy (FM), electron microscopy (EM) and soft x-ray microscopy [4–7]. For example, these studies have shown that the membrane rearrangements derive from the endoplasmic reticulum (ER) and autophagic vacuoles [8, 9]. These membranes form vesicular networks, observed during both

Received 24 April 2025; Accepted 10 October 2025; Published 06 November 2025
Author affiliations: [1]School of Molecular and Cellular Biology, Faculty of Biological Sciences, University of Leeds, Leeds LS2 9JT, UK; [2]Astbury Centre for Structural Molecular Biology, University of Leeds, Leeds LS2 9JT, UK; [3]Instituto Biofisika, CSIC-UPV/EHU, Leioa, Bizkaia 48940, Spain.
***Correspondence:** Juan Fontana, juan.fontana@csic.es; Mark Harris, m.harris@leeds.ac.uk
Keywords: cryo-electron tomography (cryo-ET); cryo-focused ion beam (cryo-FIB) milling; genome replication; hepatitis C virus (HCV); membrane vesicles.
Abbreviations: CEMOVIS, cryo-electron microscopy of vitreous sections; cryo-ET, cryo-electron tomography; cryo-FIB, cryo-focused ion beam milling; DAAs, direct-acting antivirals; DMEM, Dulbecco's modified Eagle's medium; DMV, double-membrane vesicle; EM, electron microscopy; ER, endoplasmic reticulum; ETD, Everhart-Thornley detector; FACS, fluorescence-activated cell sorting; FC7, Low temperature sectioning system for the Leica; FF-luc, firefly luciferase; FM, fluorescence microscopy; HCV, hepatitis C virus; InVs, inner vesicles; LAMP-2A, Lysosome-associated membrane protein type 2A; LD, lipid droplet; MMV, multi-membrane vesicle; MVBs, multivesicular bodies; MW, membranous web; NS, non-structural; Rab21, Ras-related protein 21; ROs, replication organelles; SEM, scanning electron microscope; SGR, subgenomic replicon; SMV, single-membrane vesicle; TEM, transmission electron microscope.
Five supplementary figures and two supplementary videos are available with the online version of this article.

viral infection and after transfection with subgenomic replicons (SGRs), which are referred to as viral replication factories or the membranous web (MW) [4, 10, 11]. The MW includes single-membrane vesicles (SMVs), double-membrane vesicles (DMVs), multi-membrane vesicles (MMVs), multivesicular bodies (MVBs) and lipid droplets (LDs) [7]. These structures have been proposed as potential replication organelles (ROs), serving as platforms for the replicase machinery.

HCV RNA replication is orchestrated by the five non-structural proteins NS3, NS4A, NS4B, NS5A and NS5B, which are necessary and sufficient to form the MW in the cytoplasm of infected or transfected cells [10, 12]. NS3/4A functions as a protease and helicase, facilitating HCV polyprotein cleavage and the unwinding of RNA secondary structures [13]. NS4B contributes to MW formation alongside NS5A [11]. NS5A is a multifunctional viral protein involved in viral replication and assembly [14]; notably, it binds NS5B and modulates its RNA-dependent RNA polymerase activity [15]. Specifically, within the MW, DMVs have been primarily hypothesized as the main HCV replication site through immunogold labelling of NS3 and NS5A. Additionally, dsRNA (a marker for RNA replication) showed colocalization with NS5A by immunofluorescence and correlated with the production of DMVs over the course of infection, further supporting DMVs as active sites of HCV RNA synthesis [7]. Furthermore, another study using an SGR containing an NS5A-mCherry fusion revealed that the majority of NS5A-positive regions (~35%) were in DMVs and MMVs [16]. However, the same studies also showed that immunogold labelling of NS3 and NS5A also localized to SMVs, LDs and ER [7], and that a relevant proportion of NS5A-mCherry regions corresponded to MVBs (~20%), ER (~7%), LDs (~7%) and mitochondria (~5%) [16]. Additionally, chronically infected liver tissue samples from patients did not present any DMVs, and the MW appeared primarily as clusters of SMVs closely associated with the ER and LDs [17]. Overall, although DMVs are suggested as the primary ROs for HCV, the type of membranous structure utilized as the major HCV replication site remains inconclusive.

To date, the EM methods employed to study cellular architecture following infection (or in SGR-harbouring cells) have yielded insights into membrane rearrangements and the roles of individual NS proteins in these processes [4, 7]. However, the sample preparation methods for visualization by EM have utilized chemical fixation, high-pressure freezing with freeze substitution, resin embedding and sectioning techniques. Therefore, we explored recent advancements in cryogenic sample preparation techniques and cryo-electron tomography (cryo-ET), which facilitate imaging under close-to-native conditions, to gain insight into the ultrastructure of these membranous structures in cells harbouring SGR. Overall, our results confirm the presence of all the above-mentioned vesicles within the HCV MW and support a model in which internal densities, potentially corresponding to viral and/or cellular components, accumulate inside inner vesicles (InVs), present inside both DMVs and SMVs, and in which NS5A-eGFP accumulates around MMVs within cells stably harbouring an HCV SGR.

METHODS

Genome sequences

The HCV genome sequence for Japanese Fulminant Hepatitis-1 (JFH-1) (genotype 2a) used in the analysis was sourced from GenBank under accession number AB047639.1. The JFH-1 subgenomic replicon (SGR) [18] was modified to replace the firefly luciferase (FF-luc) reporter with a fusion of FF-luc and neomycin phosphotransferase (termed Feo) to create the plasmid pSGR JFH-1 Feo NS3-5B [19, 20], and coding sequences for enhanced green fluorescent protein (eGFP) was inserted into NS5A-domain III (using insertion site P418) [21]. The final plasmid used in this study was SGR JFH-1 Feo NS3-5B (NS5A-eGFP), hereafter referred to as SGR-NS5A-eGFP.

Linearization of plasmid DNA for generating *in vitro* RNA transcripts

Plasmid DNA (~5 µg) was digested with XbaI (NEB) in CutSmart buffer (NEB) at 37 °C for 1 h and purified by phenol–chloroform extraction. The purified, linearized DNA (~1 µg) was used for RNA synthesis using the Ribomax Express T7 kit (Promega) and purified using an RNA Clean and Concentrator kit (Zymo Research). The RNA transcript integrity was analysed on a 1% agarose gel, and concentration was measured using a Nanodrop spectrophotometer.

Cell culture

Huh7 cells were maintained in Dulbecco's modified Eagle's medium (DMEM; Sigma) supplemented with 10% foetal bovine serum (FBS) (Gibco), 50 U ml^{-1} penicillin, 50 µg ml^{-1} streptomycin, 1% non-essential amino acids (NEAAs; Lonza) and 2.8% HEPES (Lonza). Cells were maintained in a humified incubator at 37 °C with 5% CO_2.

To generate stable SGR-NS5A-eGFP-harbouring Huh7 cells, 2 µg of replicon RNA was electroporated into 2×10^6 cells using a square-wave protocol (260 V, 25 ms). Electroporated cells were mixed with non-electroporated cells to a final density of 1.8×10^5 cells and seeded into six-well plates. After 48 h of incubation, cells were washed with PBS and subjected to selection with 700 µg ml^{-1} G418. Following multiple selection rounds, the G418 concentration was reduced to 400 µg ml^{-1} for maintenance of the polyclonal cell population.

Fluorescence microscopy

To prepare coverslips for confocal fluorescence microscopy (FM), 22 mm coverslips were cleaned with dH_2O, treated with 1 M HCl, washed, incubated in ethanol, dried and autoclaved. Control or SGR-harbouring cells (5×10^4) were seeded on coverslips or sorted by FACS for fluorescence-based selection. Sorted cells were incubated for ~21 h, fixed with 4% formaldehyde, permeabilized with 0.2% Triton X-100 and blocked with 3% bovine serum albumin in PBS (BSA-PBS). Coverslips were then stained with BODIPY dye (1:1,000), washed and mounted with ProLong Gold Antifade reagent with DAPI. Mounted slides were incubated for 2.5 h at room temperature and stored at 4 °C.

Z-stack confocal microscopy images were captured using a Zeiss LSM880 upright confocal microscope. After acquisition, the images were processed using Fiji software [22]. Wide-field fluorescent images were acquired using an EVOS microscope (Thermo Fisher Scientific).

Resin embedding and sectioning for cellular EM

Huh7 cells (control and SGR-harbouring) were trypsinized and pelleted. The resulting cell pellet was fixed with 2.5% glutaraldehyde (EM Grade; Agar Scientific) in 0.1 M sodium phosphate buffer for at least 2.5 h at room temperature. The cell pellet was washed twice for 30 min in 0.1 M sodium phosphate buffer, post-fixed with 1% osmium tetroxide in 0.1 M phosphate buffer for 1 h, and washed again twice for 30 min in the same buffer. Dehydration was achieved by incubating the pellet for 20 min in increasing concentrations of ethanol: 20%, 40%, 60%, 80% and twice in 100%. The pellet was then treated with propylene oxide twice for 20 min each. A freshly prepared resin mixture of 50% propylene oxide and 50% Araldite epoxy resin was then added to the pellet and allowed to infiltrate for several hours to overnight [23]. This was followed by infiltration with a 25% propylene oxide and 75% Araldite epoxy resin mixture for 3 h, and with 100% Araldite epoxy resin for 3–8 h. Polymerization was then carried overnight at 60 °C. Ultrathin sections (80–100 nm) were collected on slotted copper EM grids with Formvar support and stained with saturated uranyl acetate for 2 h and Reynolds lead citrate for 15 min.

Image acquisition using the FEI Tecnai T12 TEM

Cellular EM images from ultrathin sections prepared by resin embedding and sectioning were captured using an FEI Tecnai T12 Transmission Electron Microscope (TEM) operated at 120 kV.

Cell culture workflow on EM grids

For cryo-ET, Quantifoil Finder 200 mesh gold grids R1.2/1.3 (Gilder G200F1) and C-flat 200 mesh gold grids 1.2/1.3 (Electron Microscopy Sciences) were utilized. The grids were glow-discharged in a Quorum GloQube (Quorum Technologies) to enhance hydrophilicity and impart a negative charge. A negative-polarity cycle of 20 mA was applied for 30–60 s.

Next, the grids were positioned at the centre of a glass-bottom cell-culture dish (Nunc TM, 150680). Grids were functionalized with 7 µl of fibronectin (Sigma-Aldrich) at a concentration of 25 µg ml^{-1} and incubated at 37 °C for 1 h. Concurrently, FACS was performed to collect 5×10^3 and 10×10^3 cells, which were pelleted and resuspended in 50 µl of complete DMEM before being seeded onto the EM grids at various cell densities. Following a 20 min incubation at room temperature, 2 ml of complete DMEM was added to each dish, and the cells were incubated at 37 °C with 5% CO_2 for 20–24 h to promote optimal cell attachment and spread.

Plunge freezing of cells on EM grids

After culture, the cells on the EM grids were plunge-frozen using a Leica EM GP Automatic plunge freezer (Leica Microsystems) in liquid ethane at −180 °C and transferred into liquid nitrogen. To facilitate blotting, 3 µl of 1X PBS was applied to the side of the grid containing the cells, and 0.5 µl was applied to the back of the grid within the humidifier chamber. The chamber was maintained at 90% humidity and 8 °C, with blotting times adjusted between 5 and 8 s for each sample. The grids were blotted using No. 1 Whatman paper, then stored in liquid nitrogen. Subsequently, they were clipped into C-rings and placed into AutoGrids for screening and data collection compatible with the FEI Titan Krios TEM (Thermo Fisher Scientific).

Sample thinning by cryo-focused ion milling-scanning EM

The lamellae generation was carried out at the Electron Bio-Imaging Centre (eBIC) at Diamond Light Source, utilizing the scios cryo-focused ion milling-scanning EM (cryo-FIB-SEM; Thermo Fisher Scientific) and Aquilos Cryo-FIB-SEM (Thermo Fisher Scientific). Lamellae were prepared using a focused gallium ion beam on a dual-beam focused ion beam-scanning electron microscope (SEM) at a stage temperature of −180 °C. Cells located at the centre of the grid squares were selected for milling. To achieve uniform milling of the cells during the process, an organo-metallic platinum layer was applied prior to milling. This was followed by a thin layer, or splutter coat, of Pt to enhance SEM imaging. Rough milling was conducted in three gradual steps at a stage angle of 12° using a gallium beam, followed by a final fine-milling step to achieve the desired nominal thickness of the lamellae. The final beam current used when milling was performed on scios was 37 pA, while on Aquilos, it was 50 pA. Progress was monitored using SEM on the scios system (operating at 2.2–10 kV with ETD) and on the Aquilos system (operating at 2–5

kV with ETD detectors and T1 and T2 in-lens). The targeted nominal thickness for milling lamellae on the scios system was set at 200 nm, while on the Aquilos system, it was set at 160 nm.

Sample vitrification by high-pressure freezing

SGR-NS5A-eGFP cells were vitrified using a high-pressure freezing method. A suspension containing ~1×10^6 cells per millilitre was resuspended in 100 µl of cryoprotectant (20% w/v Dextran 40,000 in DMEM). The sample was placed into the 100 µm deep wells of an Au type-A specimen carrier (Leica; catalogue no. 16770152), ensuring that the wells were slightly overfilled to prevent air bubbles, and then covered with the flat side of a lipid-coated (L-α-Phosphatidylcholine; Sigma, 61771) Au type-B carrier (Leica; catalogue no. 16770153). Excess liquid was absorbed with a filter paper, and the sample was then high-pressure frozen at ~2,100 bar and −190 °C for 300 ms using a Leica EM ICE High-Pressure Freezer (Leica Microsystems).

Cryogenic FM

High-pressure frozen, cryo-preserved carriers and cryo-EM grids containing SGR-NS5A-eGFP cells were screened and imaged using a Leica THUNDER Imager EM cryo CLEM (Leica Microsystems), equipped with an HC PL APO 50x/0.9 NA cryo objective, an Orca Flash 4.0 V2 sCMOS camera (Hamamatsu Photonics), and a Solar Light Engine (Lumencor). Z-stack images were acquired with a frame size of 2,048×2,048 pixels, at 30% intensity and an exposure time of 0.2 s, utilizing LASX software (Leica Microsystems). The resulting images were processed using Fiji software [22].

Sample thinning by cryo-ultramicrotomy

High-pressure frozen samples were sectioned at cryogenic temperatures (−160 °C) using a Leica UC7 equipped with an FC7 chamber, trimming (Diatome, Trim20) and cryo-sectioning (Diatome, cryo immune, 3 mm) diamond knifes, and micromanipulators [24]. Images were captured with a stereomicroscope inside the FC7 chamber and correlated with fluorescent images obtained from the Leica THUNDER Imager (Leica Microsystems) to precisely identify regions for cryo-ET. A trapezoidal block of tissue measuring 150×100×40 µm was shaped around fluorescent targets, from which ribbons of either 70 or 40 nm thickness were produced. These ribbons were then adhered to Quantifoil R2/2, Cu 300 mesh grids (EMS) using an electrostatic gun, after the grids had been glow-discharged for 60 s at 30 mA using an Easy Glow (Cressington).

Image correlation of cryo-EM and cryo-FM maps

Maps software (Thermo Fisher Scientific) was utilized to correlate fluorescent images on-the-fly at the TEM. Low-magnification electron micrographs (atlas map: 125×, pixel size 819.2 Å, spot size 7, illuminated area 1,100 µm) were aligned based on broken grid squares and distinctive patterns embedded in the centre of Quantifoil grids. At medium magnification (overview: 580×, pixel size 224.4 Å, spot size 6, illuminated area 313 µm), specific grid squares were matched. At high magnifications (search map: 8,700×, pixel size 28.8 Å, spot size 10, illuminated area 12 µm), holes in the carbon support film served as fiducial markers to facilitate correlation. The correlation between fluorescent images and electron micrographs after tomogram collection was achieved using the MATLAB script Correlate.tex [25].

Cryo-ET

Cryo-ET was conducted using an FEI Titan Krios TEM (Thermo Fisher Scientific), operated at 300 kV and equipped with a Falcon 4i direct electron detector and a Selectris imaging filter (Thermo Fisher Scientific) in energy-filtered TEM (EFTEM) nanoprobe mode.

Single or multiple tilt series per lamella were collected. The region was selected based on how much area with cellular features was visible and suitable for tilt-series acquisition. Two different acquisition schemes were employed for imaging lamellae. The first one involved a magnification of 42,000×, corresponding to a pixel size of 3.0 Å at the specimen level, using Tomography 5.11 or 5.13 software (Thermo Fisher Scientific). A dose-symmetric acquisition scheme [26] was implemented from −60° to 60° in 2° increments, starting at an angle of 0°, maintaining a constant electron dose of ~1.5 $e^-/Å^2$ per projection, corresponding to a total dose of ~95 $e^-/Å^2$. The target defocus was between −3 and −5 µm, and an energy filter slit of 10 eV was used. Individual projections were captured in counting mode with dose fractionation. Four frames per projection were aligned and summed 'on-the-fly' using custom Python scripts that utilized commands from MotionCor2 [27] and IMOD [28] software packages. The second acquisition scheme was similar to the first one, with the following differences: the magnification employed was 64,000×, with a corresponding pixel size of 1.9 Å. The electron dose was ~2.9 $e^-/Å^2$ per projection, corresponding to a total dose of ~120 $e^-/Å^2$. The tilt range covered was from 71.2° to −46.8° in 3° increments, starting at an angle of 12.14°. Eight frames per projection were collected.

Similarly, tilt series for the cryo-ultrathin sections were collected at a magnification of 53,000×, with a corresponding pixel size of 2.40 Å. A dose-symmetric acquisition method was employed from −60° to 60° in 3° increments, maintaining a constant electron

dose of ~2.2 $e^-/Å^2$ per projection, resulting in a total electron dose of ~91 $e^-/Å^2$. The target defocus ranged from −3 to −5 µm, and an energy filter slit of 10 eV was utilized. Six frames per projection were collected.

Tomogram reconstruction

Raw images were motion-corrected using MotionCor2 [27]. The tilt-series images were aligned and reconstructed via the eTOMO interface of the IMOD software package [28]. For lamellae dataset 1, tomograms were generated using fiducial-less alignment. All tomograms were reconstructed with weighted back-projection. For lamellae dataset 2 and tomograms of cryo-ultrathin sections, reconstruction was carried out using AreTomo software [29]. All tomograms were binned four times. Tomograms from datasets 1 and 2 are presented after filtering with a three-dimensional Gaussian blur function in Fiji. For the cryo-EM of vitreous sections (CEMOVIS) dataset, images are presented without filtering.

Statistical analysis on the diameter of the vesicles

To evaluate the size of each membranous structure, identifiable vesicles and cellular features were summarized for each tomogram based on the existing literature. The data on the lamellae were collected without specific correlative guidance for the NS5A-eGFP foci, leading to the analysis of all measurable membrane structures (SMV, DMV, MMV, MVB, LD) across 112 tomograms (combined dataset). The predominant vesicles visible and measurable in the tomograms included SMVs, followed by DMVs, LDs, MVBs, MMVs and mitochondria. For each structure, both the minor and major axes were measured using IMOD's 'measure' function, with the diameter calculated by averaging these two measurements. The data were exported to GraphPad Prism for presentation.

Segmentation of membranous structures

Membranes from membranous structures in cryo-focused ion beam milling (cryo-FIB)-generated tomograms were automatically segmented using MemBrain_*seg_v10_beta* [30]. Tomograms binned at level 4 were used for membrane segmentation as input. The segmented membranes were then imported into AMIRA™ (Thermo Fisher), where membrane surfaces were colour-coded. Contents within the vesicles were segmented in AMIRA™, using a consistent threshold across the same dataset to ensure comparability. For CEMOVIS-derived tomograms, both membranes and internal vesicle content were segmented manually using AMIRA™, as automated MemBrain segmentation struggled to accurately segment MMVs.

RESULTS

Establishment and validation of SGR-harbouring cells to study HCV MW

Most ultrastructural studies examining the HCV MW have utilized the JFH-1 virus or JFH-1-SGR-NS5A-eGFP, supporting its use for structural studies [4, 5, 7, 31]. NS5A plays a critical role in both replication and assembly of the virus and is distributed as puncta throughout the cytoplasm [32], making it a key protein to track and study HCV replication.

To validate the use of SGR-NS5A-eGFP (Fig. 1a) harbouring cells for subsequent cryo-EM-based analysis, the localization of NS5A-eGFP in proximity to LDs, as previously reported [5], was confirmed by confocal microscopy (Fig. 1b). To confirm architectural differences between control Huh7 cells and those stably harbouring SGR-NS5A-eGFP, resin-embedded cell samples were sectioned, stained and imaged by TEM prior to implementing the cryo-ET workflow. Overall, noticeable differences were observed in the cellular architecture between control cells and cells harbouring SGR-NS5A-eGFP. Whereas control cells lacked any evidence of intracellular membrane reorganization, stably harbouring cells contained apparent MWs (Fig. 1c, d). Therefore, cells stably harbouring SGR-NS5A-eGFP were employed to establish *in situ* cryo-ET workflows and to gain knowledge into the organization of the different types of membranous vesicles present within the MW of HCV.

Sample preparation workflow to generate lamellae by cryo-FIB for cryo-ET

To gain insight into the architecture of the HCV MW in the SGR-NS5A-eGFP-harbouring cells under close-to-native conditions, two different approaches were explored: cryo-FIB and CEMOVIS.

To establish a cryo-FIB workflow, a homogenous population of cells harbouring SGR-NS5A-eGFP was generated by FACS, selecting for the brightest eGFP intensities (Fig. S1A, available in the online Supplementary Material). These cells were seeded onto negatively glow-discharged, fibronectin-functionalized gold grids (Fig. S1B). Since cell adherence was variable on each grid, even after functionalization, optimal cell distribution was analysed by widefield FM before selecting grids for plunge freezing (Fig. S1B, C). Subsequently, grids were screened by cryo-EM for ice thickness, and target cells suitable for cryo-FIB milling were selected (Fig. S1D). Generally, the success rate of grids with optimum cell targets and ice thickness was ~50% per session. Cryo-FIB was then performed, and the presence of LDs in the lamella, as observed through SEM imaging, confirmed that the lamella's thickness was suitable for cryo-ET imaging (Fig. S1E, F).

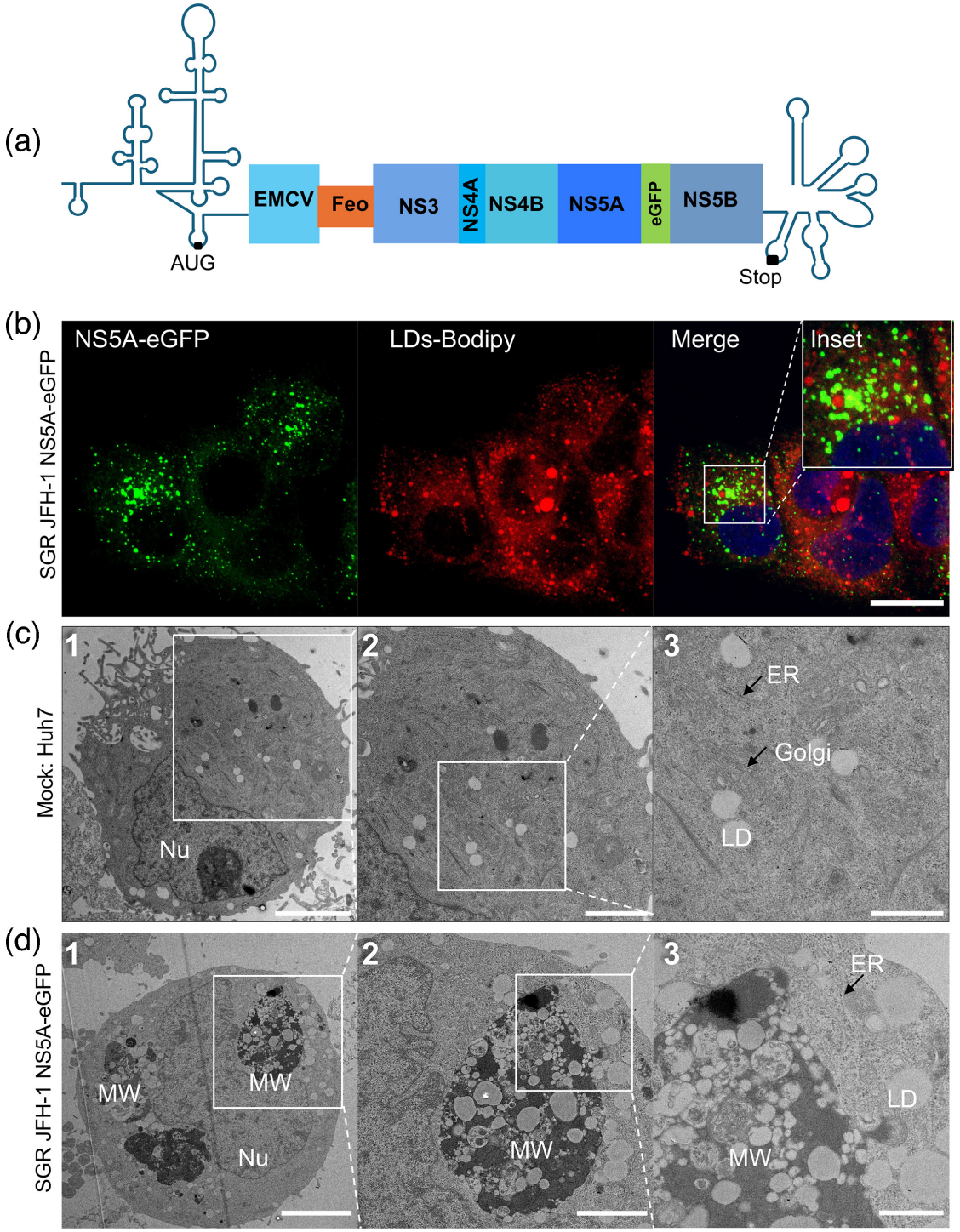

Fig. 1. Huh7 cells stably harbouring SGR-NS5A-eGFP show membrane rearrangements. (a) Schematic of the HCV SGR-NS5A-eGFP employed in this study. AUG, start codon. EMCV, Encephalomyocarditis virus (internal ribosome entry site). (b) Confocal image of Huh7 cells harbouring SGR-NS5A-eGFP. Cells were fixed with 4% formaldehyde. LDs were stained with a 1:1,000 dilution of BODIPY (558/568) for 1 h at room temperature, and nuclei were stained with ProLong Gold Antifade Mountant with DAPI. NS5A-eGFP (green), LDs (red) and nuclei of cells stained with DAPI (blue) are shown. Scale bar: 20 µm. (c) Representative TEM images of ultrathin sections of Huh7 cells and (d) Huh7 cells harbouring HCV SGR-NS5A-eGFP. Panels 1: Low magnification, panels 2: Inset of 1 (medium magnification). panels 3: Inset of 2 (high magnification). C1: TEM image acquired at nominal magnification of 2900X, D1: TEM image acquired at nominal magnification of 1900X, C2, D2: TEM image acquired at nominal magnification of 4800X, C3, D3: TEM image acquired at nominal magnification of 11000X. Scale bars: C1, 5 µm; D1, 4 µm; C2 and D2, 2 µm; C3 and D3, 1 µm. Nu, nucleus.

Quantitative and qualitative analysis of the HCV MW using a cryo-FIB/cryo-ET workflow

To investigate the native architecture of the different membranous vesicles within the MW of SGR-NS5A-eGFP-harbouring cells, cryo-ET was applied to the lamellae. To locate regions for tilt-series acquisition, search maps were utilized (Fig. 2a), looking for areas containing MWs. A total of 112 reconstructed tomograms from two datasets were analysed. MVBs were present in 50% of these, SMVs in 39%, DMVs in 29%, LDs in 15%, ER in 12%, MMVs in 11%, extensive MW in 9% and mitochondria in 5%.

Based on the hypothesis that DMVs are the main sites of replication [7, 33], the initial investigation centred on studying the ultrastructure of DMVs and their surrounding environment. DMVs were often surrounded by double-membraned tubules [e.g. see Fig. 2b-1], SMVs and MVBs. Most of the DMVs examined had a closed configuration [i.e. no pores connecting the inside of the DMVs to the cytoplasm were observed; Fig. 2b-1], with only one instance (1 out of 112 tomograms, consisting of two open DMVs) exhibiting an aperture facing towards the cytosol [Fig. 2b-2]. The reconstructed tomogram is shown in Video S1.

As an initial characterization of the different vesicles, the maximum diameter of all membranous structures that were clearly visible (n=199) was measured (Fig. 2c). The majority of SMVs, DMVs and InVs (found within DMVs and SMVs) had diameters between 50 and 300 nm, while LDs displayed a wider range of diameter, ranging from 100 to 500 nm. MVBs, the most abundant type of vesicles imaged in the datasets, were much larger and mostly above 400 nm in diameter. However, their larger size rendered them only partially visible within the tomograms, making it challenging to accurately measure their diameter. For this reason, the diameter of only 20 MVBs was measured. MMVs were observed in only 11 tomograms; however, only three MMVs could be measured and had diameters similar to that of MVBs.

Next, differences in the general distribution of densities within DMVs and SMVs were examined. Most DMVs (93%) either contained faint densities that could be a result of the inherent noise within the cryo-electron tomograms or appeared empty [exemplars in Fig. 3a-1, 2 and Fig. S2A]. Seven per cent of DMVs contained patches of density on the inside of the membrane [exemplars in Fig. 3a-3, 3b-1 and Fig. S2B]. We postulate that these could represent replicase components; however, we have no direct evidence to support this conjecture. Finally, 18% of DMVs contained an InV [either a single or double membrane; see exemplars in Fig. 3b-1, 2, 3 and Fig. S2B].

On the other hand, most SMVs [51%; Fig. 3c-1, 3d-1] contained faint densities or appeared empty, making it difficult to confirm their contents, whereas 28% contained homogeneous density throughout the vesicle [Fig. 3c-2]. Only 33% of SMVs contained patches of density [Fig. 3c-3], again potentially consistent with the presence of either cellular or viral proteins. Similar to DMVs, 19% of SMVs contained InVs [Fig. 3d-1, 2, 3)]. Out of 31 InVs measured for diameter (6 inside DMVs and 20 inside SMVs), 38% of them contained densities, 32% of them could not be confirmed but possibly have densities and 25% of them appeared empty. Exemplars of segmented membranes and their contents within them are shown in Fig. 4.

Previous reports by immunogold labelling suggested that both NS3 and NS5A primarily labelled rER and SMVs of 50–70 nm diameter, and to a lesser extent DMVs [7]. Consistent with this, we propose that the presence of densities within DMV and SMV seen here could potentially represent replication complexes containing NS3 and NS5A. Strikingly, the only membranous structures containing a significant percentage of inner densities were InVs.

NS5A-eGFP preferentially locates around MMVs

We were unable to directly correlate the replicase machinery within specific membrane structures using the cryo-FIB-milled cryo-ET datasets, due to limitations in utilising NS5A-eGFP fluorescence for guided tilt-series collection on the lamellae. Therefore, we developed an alternative workflow incorporating CEMOVIS. This approach aimed to gather evidence regarding the types of structures proximal to NS5A that potentially housed the replication complex in cells stably harbouring SGR-NS5A-eGFP (Fig. S4). An advantage of this approach was its ability to employ a heterogeneous population of SGR-NS5A-eGFP cells, thereby eliminating the need for FACS sorting. NS5A-eGFP puncta were detectable in cryo-ultrathin sections following cryo-ultramicrotomy and could thus serve as markers for guided tilt-series acquisition.

Using this approach, ultrathin sections of varying thicknesses (40, 70 and 100 nm) were evaluated, with the 40 nm sections displaying clear cellular features, whereas the thicker sections exhibited low contrast. Therefore, 12 tilt series were collected from a single 40 nm section, guided by NS5A-eGFP foci, and subsequently correlated (Fig. 5a).

Reconstructed tomograms from 12 NS5A-eGFP tilt series were quantified with respect to the various membrane structures they contained: 83.3% were MMVs, 33.3% ER, 25% DMVs, 25% mitochondria, 16.6% LD and 8.3% MVB. Twelve tomograms primarily revealed 39 MMVs with notable densities inside (four of which are illustrated in Fig. 5b–e, and other examples in Fig. S5), with only three DMVs identified. Similar densities were observed within and around DMVs, as noted in the cryo-FIB-milled dataset. Interestingly, the proportion of DMVs and MMVs was reversed between tomograms obtained using the CEMOVIS and cryo-FIB workflows. In the cryo-FIB datasets, which were not guided by NS5A-eGFP presence, DMVs were more prevalent, comprising 13% of the vesicles (27 DMVs out of 199 structures measured). In contrast, MMVs dominated in the CEMOVIS datasets, comprising 80% of the vesicles (39 MMVs out of 49 structures identified), which were exclusively collected in regions exhibiting NS5A-eGFP signals. Again, we observed that one of the MMVs (Fig. 5e) displayed heterogeneous densities, consistent

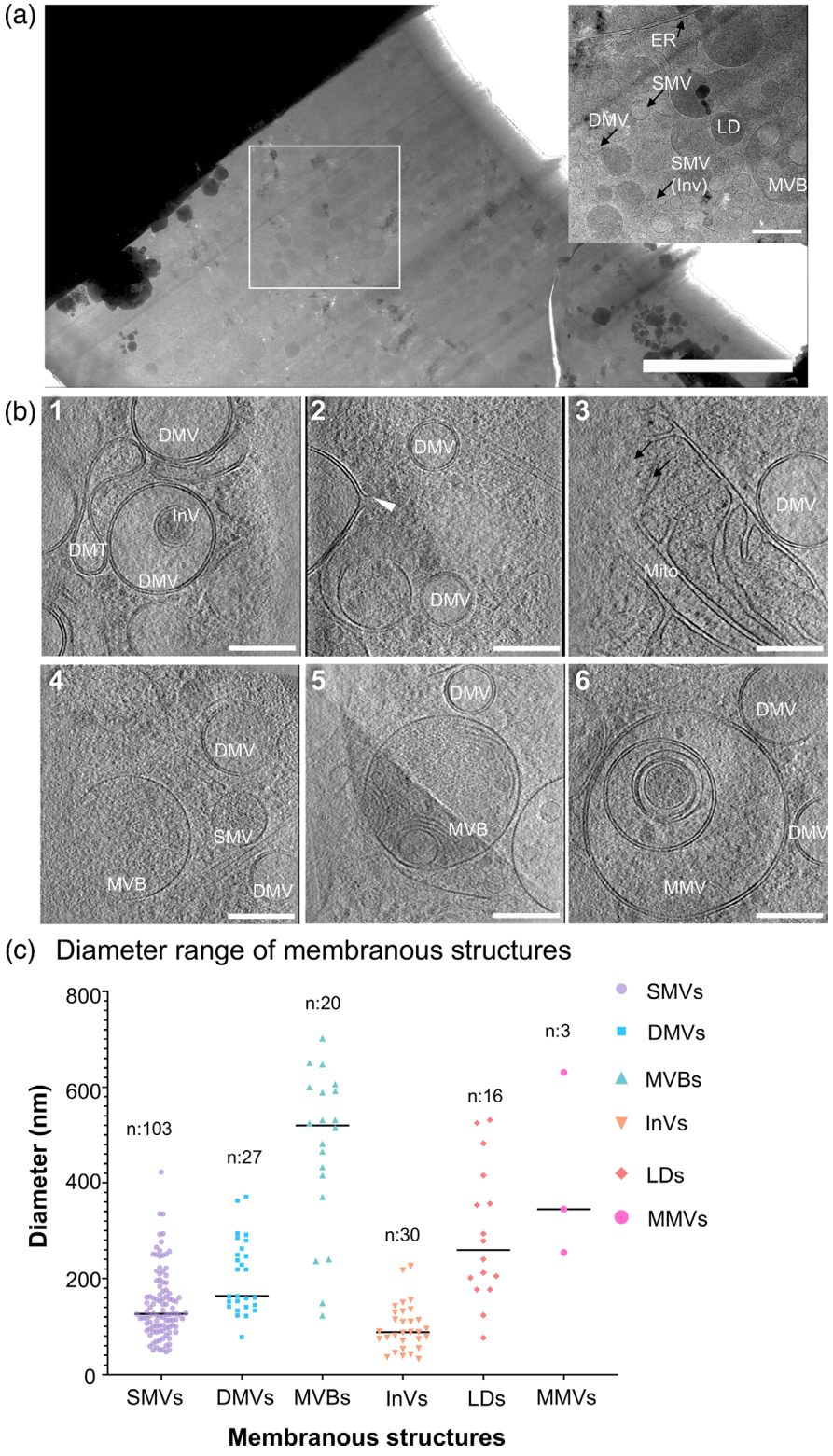

Fig. 2. HCV membranous structures imaged by cryo-FIB/cryo-ET in Huh7 cells harbouring SGR-NS5A-eGFP. (a) Representative search map (magnification 15,000×) of a lamella containing membranous structures around LDs. An area highlighting specific structures is shown in the inset. Scale bars: search map, 2 µm; inset, 500 nm. (b) Representative sections through reconstructed tomograms showing the architecture of HCV MW. Scale bars: 200 nm. The white arrow indicates the opening of a DMV towards the cytosol. (c) Graph depicting the diameters of the 199 observed membranous structures. DMT, double-membraned tubule; Mito, mitochondria.

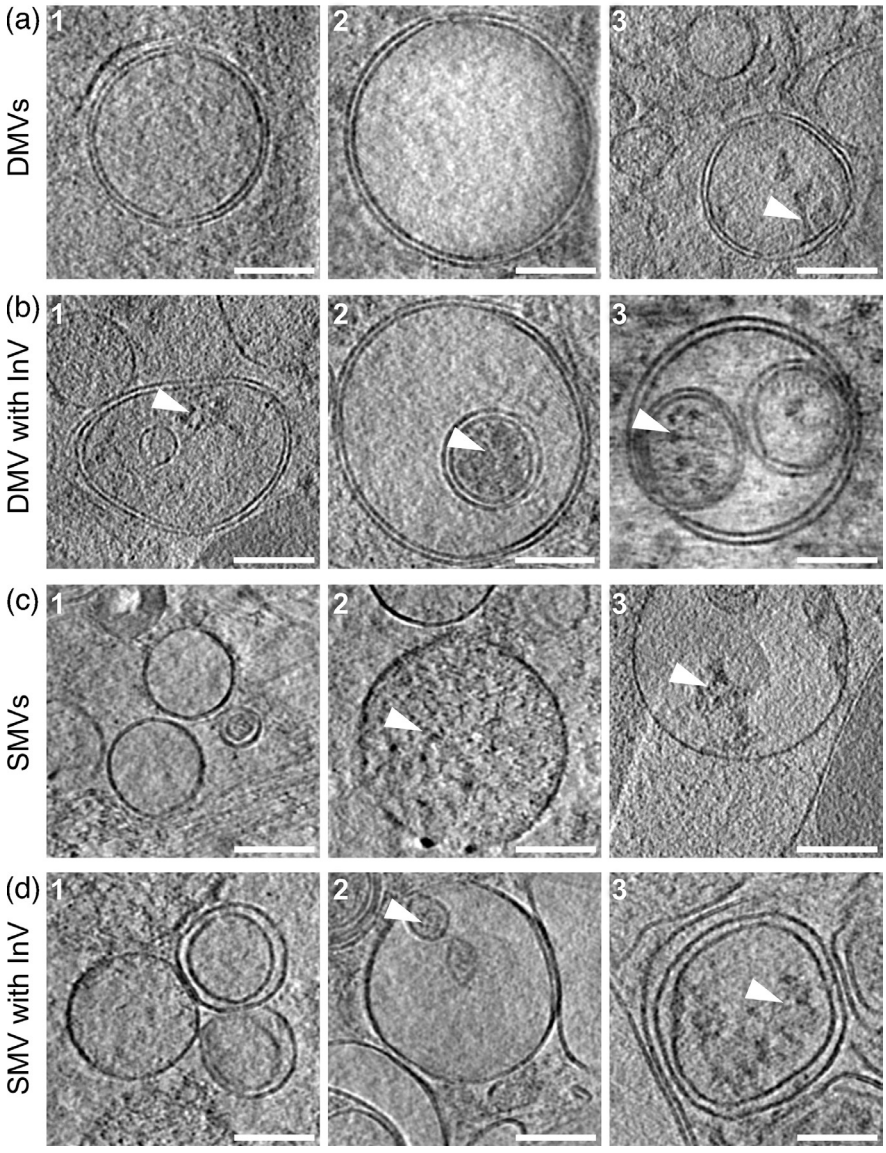

Fig. 3. Differences in densities present within DMVs and SMVs. (a) Representative tomographic slices showing differences in the contents within DMVs. (b) Representative tomographic slices showing InVs within DMVs and their contents. (c) Representative tomographic slices showing differences in the contents within SMVs. (d) Representative tomographic slices showing InVs within SMVs and their contents. Scale bars: A1,2; B2,3; C1,2 and D1,2,3:100 nm; A3, B1 and C3:160 nm. White arrows indicate densities present within the vesicles.

with the presence of cellular or viral proteins such as the HCV replication complex. The reconstructed tomogram is shown in video S2. Notably, this represents the most organized assembly of cryo-densities observed across all datasets, underscoring the value of fluorescence-guided tilt-series collection on thin cryo-specimens. Exemplars of segmented membranes and contents within them are shown in Fig. 6.

DISCUSSION

Over the past decade, the use of direct-acting antivirals (DAAs) has dramatically improved the lives of patients with HCV infection. The targets for DAAs (NS3 protease, NS5A and NS5B RNA-dependent RNA polymerase) are all directly involved in virus genome replication, and it is thus important to understand the molecular details of this process to shed light on the mode of action of DAAs and contribute to understanding DAA resistance. In this regard, one important avenue of research has focused on understanding how HCV modifies cytoplasmic membranes to host the genome replication complex. Numerous studies have examined membranous structures within the MW in either infected cells or those harbouring SGR, using a mix of

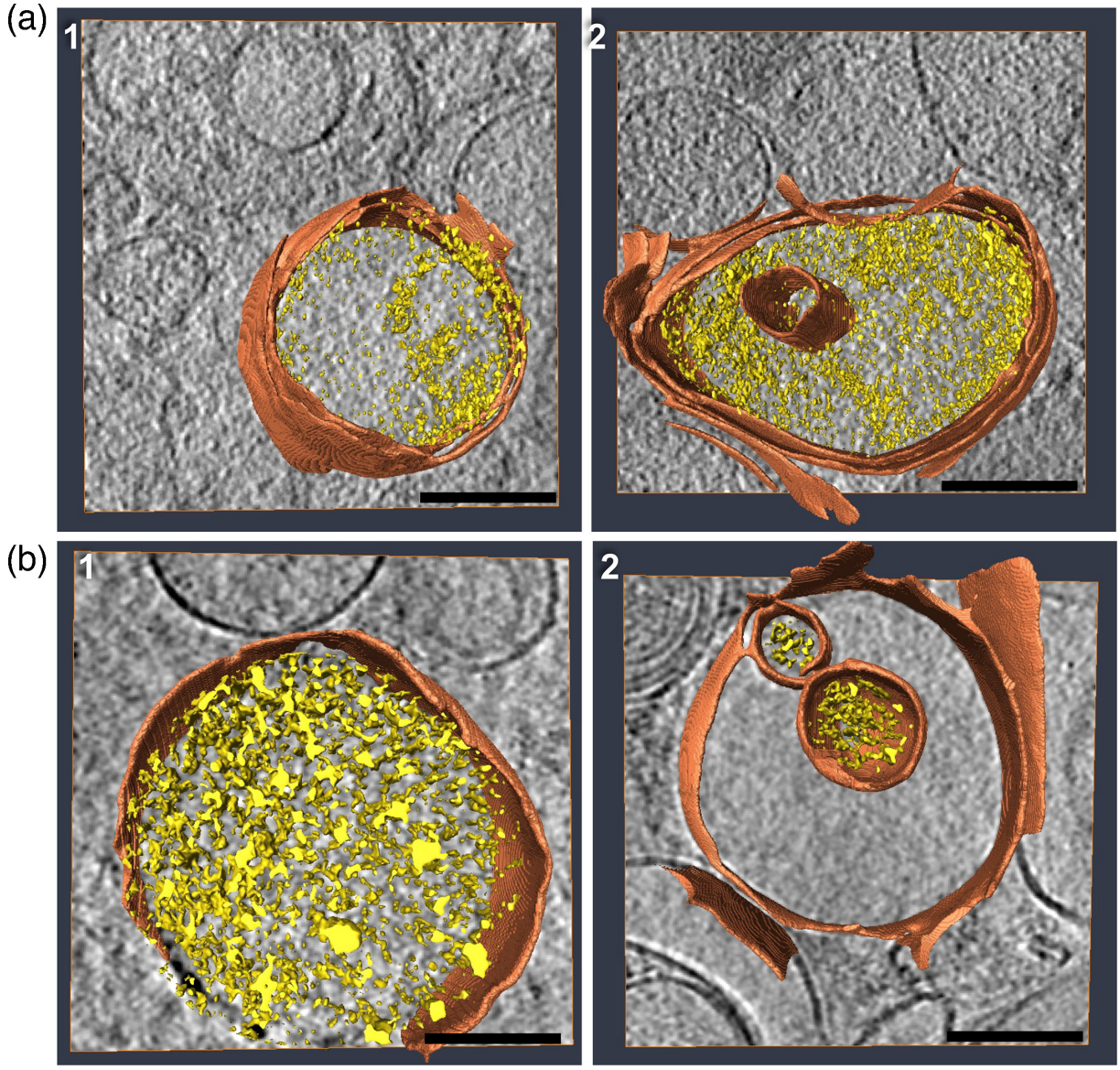

Fig. 4. Representative 3D segmented membrane surfaces and contents within DMVs and SMVs. (a) (1) Representative 3D segmented surface of a DMV [corresponding to Fig. 3a(3)] and (2) DMV with InV [corresponding to Fig. 3b(1)]. Scale bar: 160 nm. (b) (1) Representative 3D segmented surface of a SMV [corresponding to Fig. 3c(2)] and (2) SMV with InV [corresponding to Fig. 3d(2)]. Scale bars: 100 nm. Membranes were auto-segmented by MemBrain segmentation software. Content shown within the vesicles was segmented and thresholded using AMIRA™. The threshold for content was kept at the same value for A1,2 (same dataset) and then B1,2 (same dataset). Vesicles are coloured in brown, and their contents are coloured in yellow. 3D, three-dimensional.

light and EM techniques [4–9, 34]. However, these studies relied on chemical fixatives and resin-embedded sections, limiting the direct visualization of key replication components such as dsRNA and protein arrangements within membranous structures. Furthermore, even though DMVs have been identified as the most probable structures to harbour the replication complex [7], the location of the replication complex is still under debate due to the lack of direct visualization of the assembly of viral and cellular proteins. Here, we developed a detailed workflow incorporating the latest cryo-ET techniques and established two cryogenic sample-preparation techniques for an investigation of the membranous structures in Huh7 cells stably harbouring an SGR (HCV genotype 2a): cryo-FIB milling [35] and CEMOVIS [36].

In SGR-harbouring cells, host membrane modifications similar to those in HCV-infected cells were observed [7]. To track viral proteins, we utilized SGR-NS5A-eGFP, as NS5A is the only HCV non-structural protein that can be fluorescently tagged and retain functionality. However, one limitation of this approach is that NS5A is involved in both replication and assembly [32], suggesting that some observed NS5A-eGFP signals may not be exclusively associated with replication sites.

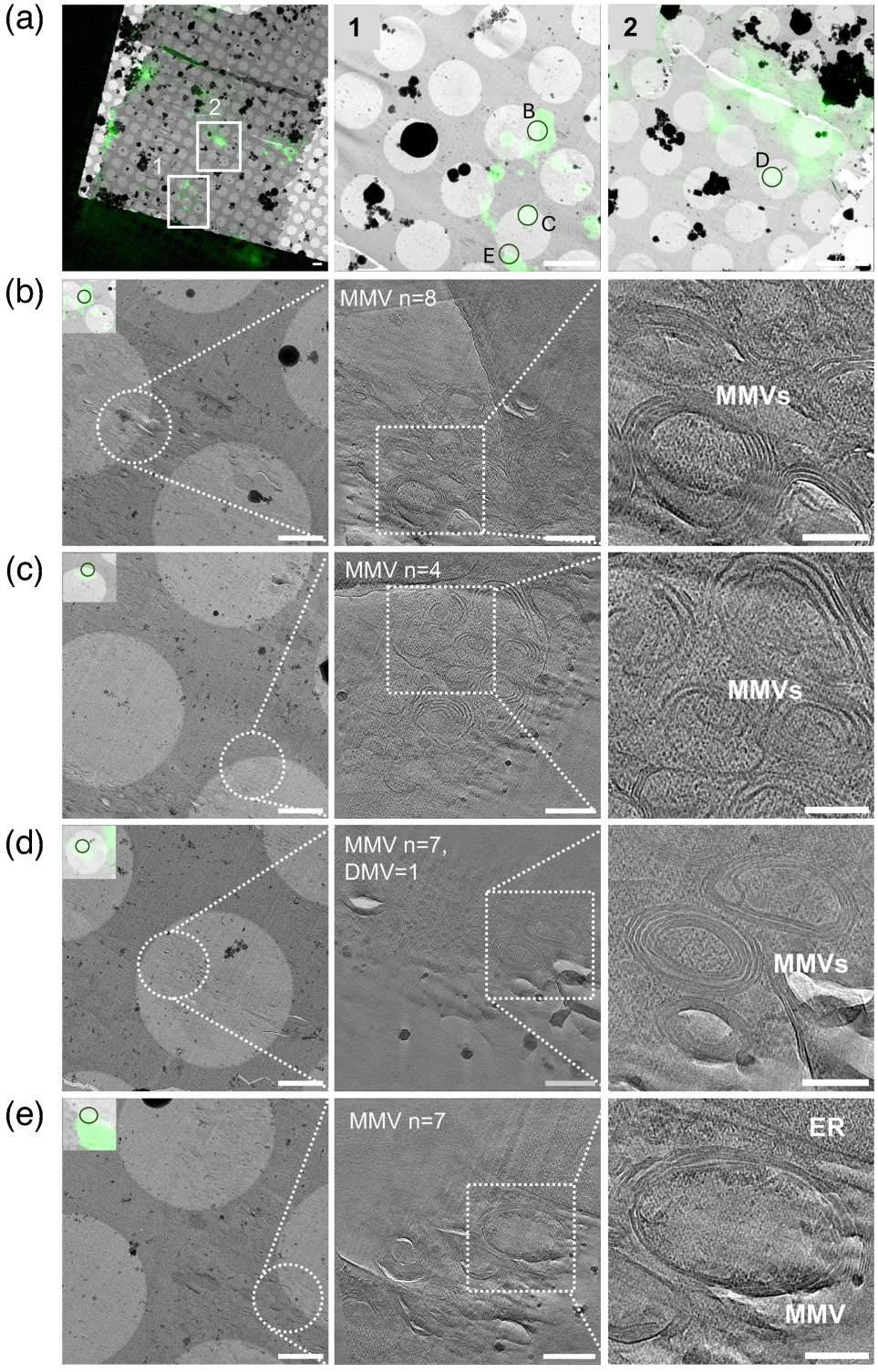

Fig. 5. NS5A-eGFP-guided acquisition of HCV MW observed in Huh7 cells stably harbouring SGR-NS5A-eGFP by CEMOVIS and cryo-ET. (a) Left, low-magnification search map (125×) of a 40 nm cryo-ultrathin ribbon with regions of NS5A-eGFP signal shown in white boxes. Centre and right, areas of NS5A-eGFP foci used for tilt-series collection are shown with green circles and labelled with designated letters that correspond to the search maps and tomograms below. Scale bar: 2 µm. (b–e) Left, cryo-EM search map (580×) with highlighted position by a white circle where the tilt series was acquired. Centre and right, tomographic sections at low (centre) and high magnification (right) of membranous structures observed in the tomograms acquired at the specified NS5A-eGFP signals. Scale bars: left, 1 µm; centre, 200 nm; right, 100 nm.

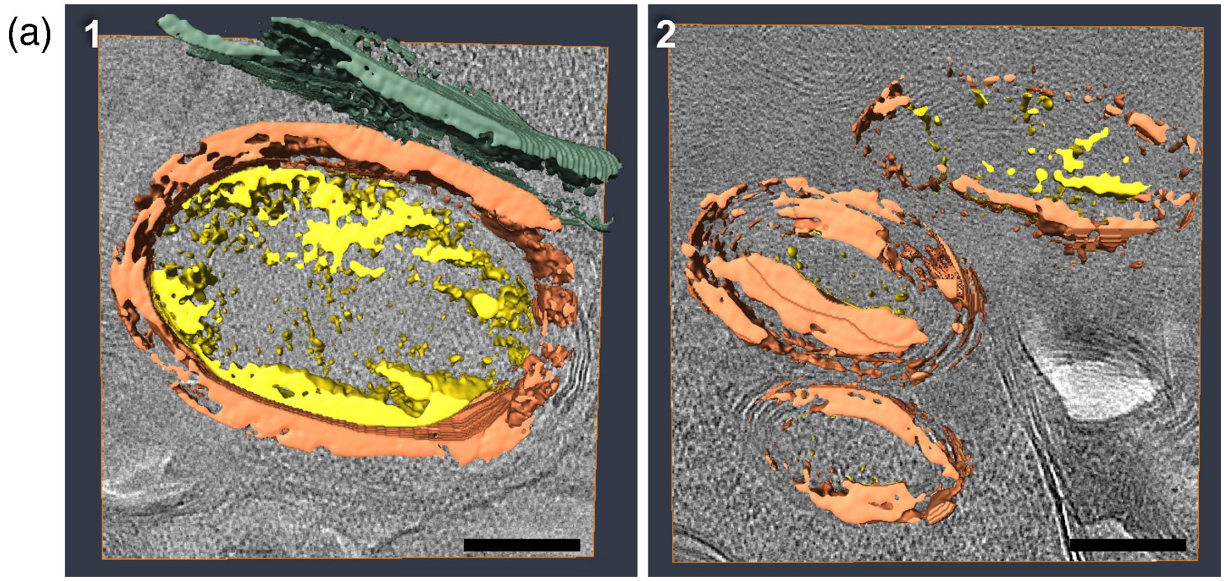

Fig. 6. Representative 3D segmented membrane surface and content within MMV. (a) (1) Corresponding to Fig. 5e and (2) corresponding to Fig. 5d. Scale bars: 100 nm. Membranes were segmented using AMIRA™, and the content shown within the vesicles was thresholded using AMIRA™. The threshold for content was kept at the same value for A1,2 (same dataset). Vesicles are coloured in brown; content is coloured in yellow and ER is coloured in green.

Datasets acquired using cryo-FIB milling followed by cryo-ET [37], without fluorescence guidance, enabled the exploration of the MW induced by SGR-NS5A-eGFP in Huh7 cells. Analysis of these datasets revealed numerous DMVs and SMVs. While more data are required to confirm our conclusions, the limited examples provided here show that most DMVs appeared empty or contained densities at background levels, whereas SMVs frequently exhibited either patchy densities or were entirely filled. Additionally, both DMVs and SMVs occasionally contained InVs with densities present within. These InVs have been previously described as self-invaginations of SMVs [7] or vesicles in cluster [31]. However, they may also represent exosomes containing dsRNA or non-structural proteins that fuse with larger vesicles, potentially serving as replication sites [38–40]. Given that positive-sense RNA virus replication sites are expected to contain viral replicase and RNA [3], our findings suggest that SMVs and InVs may serve as primary sites for HCV SGR replication. This is further supported by EM studies of chronically infected HCV patient cells, which identified SMVs, and not DMVs, around LDs and the ER [17].

In any case, the most frequently observed vesicles in the cryo-FIB/cryo-ET dataset were MVBs, consistent with EM analysis of replicon cells transiently transfected with an SGR expressing NS5A-mCherry [16], suggesting their involvement in the process of replication. The aggregations of MVBs, found primarily near SMVs, DMVs and LDs, with diameter sizes ranging from 400 to 800 nm (though most exceeded 1,000 nm) were previously described as single-membrane compartments containing multiple circular units with dense cores [4]. The presence of densities within SMVs and DMVs within MVBs also aligns with the previous observations of NS5A-mCherry localized inside MVBs [16], and with the dense lumen within concentric units [4]. The smaller SMVs (30–150 nm) observed within MVBs resemble exosomes in size. Previous studies have demonstrated that exosomes derived from HCV-infected cells contain viral RNA, proteins and complete virions [40]. Notably, these exosomes facilitate the transfer of HCV RNA to uninfected cells, even in the presence of neutralizing antibodies [39]. This suggests that MVBs play a role in HCV RNA dissemination. On rare instances, tomograms captured SMVs invaginating into MVBs [Fig. S3(1)], supporting the hypothesis that MVBs may transport vesicles containing replicase machinery or dsRNA to neighbouring cells [16]. Perhaps, the accumulation of MVBs in SGR-harbouring cells is due to the lack of viral assembly in this system, thus depriving nascent genomic RNA of a 'final destination'. Nonetheless, this observation suggests a potential role for MVBs in HCV replication.

In contrast to the cryo-FIB/cryo-ET dataset, CEMOVIS guided by NS5A-eGFP fluorescence revealed the accumulation of MMVs (Fig. 5). Indeed, the most abundant vesicles in the CEMOVIS datasets were MMVs, suggesting that these are the sites of genome replication. Intriguingly, one tomogram revealed densities arranged in a regular pattern, potentially representing replicase machinery assembly on the inner leaflet of an MMV (Fig. 5e). The predominance of NS5A-eGFP associated with MMVs in the CEMOVIS dataset does conflict with the study by Grünvogel *et al.* [16], however, this might be due to differences in both cells (transiently transfected Huh7-Lunet cells compared to stably SGR-harbouring Huh7 cells) or procedures (correlative light and electron microscopy compared to CEMOVIS).

One point of interest is the notable absence of pores in the observed membrane structures; indeed, only one was observed throughout the entire dataset [Fig. 2b-2], and this example appeared to span only the outer of the two membranes in a DMV. Conceptually, a pore is required for the import of NTPs and the export of nascent genomic RNA; however, this might be a transient structure, possibly explaining its absence in these images. Additionally, making the assumption that there is only one pore per DMV, the pore will take up a very small proportion of the total surface area. In the example, the DMV had a diameter of ~400 nm, and the pore was ~25 nm in diameter. The pore would thus be 0.09% of the total surface area, and this may also explain the lack of observed pores in the dataset.

Previous immunofluorescence studies indicated that HCV replication vesicle membranes originate from the ER but also colocalize with markers of early and late endosomes, coat protein complex vesicles, mitochondria and LDs [7], as well as lysosomes [41]. The measured SMV diameter (50–300 nm) aligns with those of endosomes (100–500 nm) and lysosomes (200–300 nm). If these SMVs are derived from early endosomes, their internal densities may represent NS3 and NS5A, while surface-exposed densities may correspond to GFP-Rab21 [7]. Alternatively, if they originate from lysosomes, internal densities may include NS5A and LAMP-2A [41].

In conclusion, these findings provide new insights into the spatial organization of NS or cellular proteins within membranous structures in replicon-transfected cells, revealing structural details previously inaccessible through conventional EM. As cryo-ET continues to evolve with advancing computational techniques, it will further refine our understanding of NS-protein interactions with cellular proteins and HCV RNA genome organization within these membranous structures.

Funding information
U.M.S. was supported by a Wellcome PhD studentship (222370/Z/21/Z). HCV studies in the MH laboratory were supported by a Wellcome Investigator Award (096670/Z/11/Z) and an MRC project grant (MR/S001026/1). J.F. was supported by grant PID2023-149259NB-I00, funded by MICIU/AEI/10.13039/501100011033 and by 'ERDF A way of making Europe'. The funders had no role in study design, data collection and analysis, decision to publish or preparation of the manuscript.

Acknowledgements
We acknowledge the technical contributions of the University of Leeds Bioimaging Facility, especially Dr Ruth Hughes and Dr Sally Boxall; the Astbury Biostructure Laboratory Electron Microscopy facility, especially Mr Martin Fuller and Dr Rebecca Thompson; and the Electron BioImaging Centre (eBIC) at Diamond Light Source, especially Dr James Gilchrist.

Author contributions
U.M.S., J.F. and M.H.: Planned the study and wrote the main manuscript text. U.M.S., T.J.O'S. and Y.H.: Performed the experiments. U.M.S. and J.F.: Analysed the data. All authors reviewed the manuscript.

Conflicts of interest
The authors declare that there are no conflicts of interest.

References

1. Sykora UM, O'Sullivan TJ, Halfon Y, Fontana J, Harris M. The architecture of membrane structures involved in hepatitis c virus genome replication revealed in close-to-native conditions by cryo-electron tomography. *Figshare* 2025. DOI: 10.6084/m9.figshare.30306745.
2. Martinello M, Solomon SS, Terrault NA, Dore GJ. Hepatitis C. *Lancet* 2023;402:1085–1096.
3. Wolff G, Melia CE, Snijder EJ, Bárcena M. Double-membrane vesicles as platforms for viral replication. *Trends Microbiol* 2020;28:1022–1033.
4. Ferraris P, Blanchard E, Roingeard P. Ultrastructural and biochemical analyses of hepatitis C virus-associated host cell membranes. *J Gen Virol* 2010;91:2230–2237.
5. Lee J-Y, Cortese M, Haselmann U, Tabata K, Romero-Brey I, *et al*. Spatiotemporal Coupling of the Hepatitis C Virus Replication Cycle by Creating a Lipid Droplet- Proximal Membranous Replication Compartment. *Cell Rep* 2019;27:3602–3617.
6. Paul D, Madan V, Bartenschlager R. Hepatitis C virus RNA replication and assembly: living on the fat of the land. *Cell Host & Microbe* 2014;16:569–579.
7. Romero-Brey I, Merz A, Chiramel A, Lee JY, Chlanda P, *et al*. Three-dimensional architecture and biogenesis of membrane structures associated with hepatitis C virus replication. *PLoS Pathog* 2012;8:e1003056.
8. Mohl B-P, Bartlett C, Mankouri J, Harris M. Early events in the generation of autophagosomes are required for the formation of membrane structures involved in hepatitis C virus genome replication. *J Gen Virol* 2016;97:680–693.
9. Pérez-Berná AJ, Rodríguez MJ, Chichón FJ, Friesland MF, Sorrentino A, *et al*. Structural changes in cells imaged by soft X-ray cryo-tomography during hepatitis C virus infection. *ACS Nano* 2016;10:6597–6611.
10. Gosert R, Egger D, Lohmann V, Bartenschlager R, Blum HE, *et al*. Identification of the hepatitis C virus RNA replication complex in Huh-7 cells harboring subgenomic replicons. *J Virol* 2003;77:5487–5492.
11. Moradpour D, Gosert R, Egger D, Penin F, Blum HE, *et al*. Membrane association of hepatitis C virus nonstructural proteins and identification of the membrane alteration that harbors the viral replication complex. *Antiviral Res* 2003;60:103–109.
12. Lohmann V, Körner F, Koch J-O, Herian U, Theilmann L, *et al*. Replication of subgenomic hepatitis C virus RNAs in a hepatoma cell line. *Science* 1999;285:110–113.
13. Bartenschlager R, Lohmann V, Wilkinson T, Koch JO. Complex formation between the NS3 serine-type proteinase of the hepatitis C virus and NS4A and its importance for polyprotein maturation. *J Virol* 1995;69:7519–7528.
14. Hughes M, Griffin S, Harris M. Domain III of NS5A contributes to both RNA replication and assembly of hepatitis C virus particles. *J Gen Virol* 2009;90:1329–1334.
15. Shirota Y, Luo H, Qin W, Kaneko S, Yamashita T, *et al*. Hepatitis C virus (HCV) NS5A binds RNA-dependent RNA polymerase (RdRP) NS5B and modulates RNA-dependent RNA polymerase activity. *J Biol Chem* 2002;277:11149–11155.

16. Grünvogel O, Colasanti O, Lee J-Y, Klöss V, Belouzard S, *et al*. Secretion of hepatitis C virus replication intermediates reduces activation of toll-like receptor 3 in hepatocytes. *Gastroenterology* 2018;154:2237–2251.
17. Blanchard E, Roingeard P. The hepatitis C virus-induced membranous web in liver tissue. *Cells* 2018;7:11.
18. Wakita T, Pietschmann T, Kato T, Date T, Miyamoto M, *et al*. Production of infectious hepatitis C virus in tissue culture from a cloned viral genome. *Nat Med* 2005;11:791–796.
19. Ross-Thriepland D, Mankouri J, Harris M. Serine phosphorylation of the hepatitis C virus NS5A protein controls the establishment of replication complexes. *J Virol* 2015;89:3123–3135.
20. Wyles DL, Kaihara KA, Korba BE, Schooley RT, Beadle JR, *et al*. The octadecyloxyethyl ester of (S)-9-[3-hydroxy-2-(phosphonomethoxy) propyl]adenine is a potent and selective inhibitor of hepatitis C virus replication in genotype 1A, 1B, and 2A replicons. *Antimicrob Agents Chemother* 2009;53:2660–2662.
21. Moradpour D, Evans MJ, Gosert R, Yuan Z, Blum HE, *et al*. Insertion of green fluorescent protein into nonstructural protein 5A allows direct visualization of functional hepatitis C virus replication complexes. *J Virol* 2004;78:7400–7409.
22. Schindelin J, Arganda-Carreras I, Frise E, Kaynig V, Longair M, *et al*. Fiji: an open-source platform for biological-image analysis. *Nat Methods* 2012;9:676–682.
23. Luft JH. Improvements in epoxy resin embedding methods. *J Biophys Biochem Cytol* 1961;9:409–414.
24. Studer D, Klein A, Iacovache I, Gnaegi H, Zuber B. A new tool based on two micromanipulators facilitates the handling of ultrathin cryosection ribbons. *J Struct Biol* 2014;185:125–128.
25. Schorb M, Briggs JAG. Correlated cryo-fluorescence and cryo-electron microscopy with high spatial precision and improved sensitivity. *Ultramicroscopy* 2014;143:24–32.
26. Hagen WJH, Wan W, Briggs JAG. Implementation of a cryo-electron tomography tilt-scheme optimized for high resolution subtomogram averaging. *J Struct Biol* 2017;197:191–198.
27. Zheng SQ, Palovcak E, Armache J-P, Verba KA, Cheng Y, *et al*. MotionCor2: anisotropic correction of beam-induced motion for improved cryo-electron microscopy. *Nat Methods* 2017;14:331–332.
28. Kremer JR, Mastronarde DN, McIntosh JR. Computer visualization of three-dimensional image data using IMOD. *J Struct Biol* 1996;116:71–76.
29. Zheng S, Wolff G, Greenan G, Chen Z, Faas FGA, *et al*. AreTomo: an integrated software package for automated marker-free, motion-corrected cryo-electron tomographic alignment and reconstruction. *Journal of Structural Biology: X* 2022;6:100068.
30. Lamm L, Zufferey S, Zhang H, Righetto RD, Waltz F, *et al*. MemBrain v2: an end-to-end tool for the analysis of membranes in cryo-electron tomography. *Bioinformatics* 2024. DOI: 10.1101/2024.01.05.574336.
31. Ferraris P, Beaumont E, Uzbekov R, Brand D, Gaillard J, *et al*. Sequential biogenesis of host cell membrane rearrangements induced by hepatitis C virus infection. *Cell Mol Life Sci* 2013;70:1297–1306.
32. Eyre NS, Fiches GN, Aloia AL, Helbig KJ, McCartney EM, *et al*. Dynamic imaging of the hepatitis C virus NS5A protein during a productive infection. *J Virol* 2014;88:3636–3652.
33. Romero-Brey I, Bartenschlager R. Viral infection at high magnification: 3D electron microscopy methods to analyze the architecture of infected cells. *Viruses* 2015;7:6316–6345.
34. Berger C, Romero-Brey I, Radujkovic D, Terreux R, Zayas M, *et al*. Daclatasvir-like inhibitors of NS5A block early biogenesis of hepatitis C virus-induced membranous replication factories, independent of RNA replication. *Gastroenterology* 2014;147:1094–105..
35. Lam V, Villa E. Practical Approaches for Cryo-FIB Milling and Applications for Cellular Cryo-Electron Tomography BT - cryoEM: Methods and Protocols. In: Gonen T and Nannenga BL (eds). *CryoEM Methods and Protocols*. New York, NY: Humana; 2021. pp. 49–82.
36. Chlanda P, Sachse M. Cryo-electron microscopy of vitreous sections. *Methods Mol Biol* 2014;1117:193–214.
37. Wagner FR, Watanabe R, Schampers R, Singh D, Persoon H, *et al*. Preparing samples from whole cells using focused-ion-beam milling for cryo-electron tomography. *Nat Protoc* 2020;15:2041–2070.
38. Bukong TN, Momen-Heravi F, Kodys K, Bala S, Szabo G. Exosomes from hepatitis C infected patients transmit HCV infection and contain replication competent viral RNA in complex with Ago2-miR122-HSP90. *PLoS Pathog* 2014;10:e1004424.
39. Ramakrishnaiah V, Thumann C, Fofana I, Habersetzer F, Pan Q, *et al*. Exosome-mediated transmission of hepatitis C virus between human hepatoma Huh7.5 cells. *Proc Natl Acad Sci U S A* 2013;110:13109–13113.
40. Yin Y, Zhao Y, Chen Q, Chen Y, Mao L. Dual roles and potential applications of exosomes in HCV infections. *Front Microbiol* 2022;13:1044832.
41. Matsui C, Yuliandari P, Deng L, Abe T, Shoji I. The role of chaperone-mediated autophagy in hepatitis C virus-induced pathogenesis. *Front Cell Infect Microbiol* 2021;11:796664.